International Symposium
On Turbulence and Shear Flow
Phenomena (TSFP-9)
June 30 - July 3, 2015 *Melbourne, Australia*

TURBULENT STRUCTURES IN A NON-EQUILIBRIUM LARGE-VELOCITY-DEFECT TURBULENT BOUNDARY LAYER

Yvan Maciel
Department of Mechanical Engineering
Laval University
Quebec City, QC, G1V 0A6 Canada
yvan.maciel@gmc.ulaval.ca

Mark P. Simens
School of Aeronautics
Universidad Politécnica de Madrid
28040 Madrid, Spain
markphilsimens@gmail.com

Ayse G. Gungor
Faculty of Aeronautics and Astronautics
Istanbul Technical University
34469 Maslak, Istanbul, Turkey
ayse.gungor@itu.edu.tr

ABSTRACT

The characteristics of three-dimensional intense *uv* coherent structures (Qs) in a strongly decelerated large-velocity-defect boundary layer are analysed by direct numerical simulation. The Reynolds number close to the exit is $Re_\theta = 2175$ and the shape factor $H = 2.5$. In the region of large-velocity-defect flow, the maxima of Reynolds stresses and of production of turbulent kinetic energy are located in the middle of the boundary layer. The Q2 and Q4 structures are found to be different from those of turbulent channel flows studied by Lozano-Durán et al. (J. Fluid Mech., vol. 694, 2012). They are less streamwise elongated and less present near the wall. Moreover, contrary to channel flows, wall-detached Q2 and Q4 structures are more frequent and carry a much larger amount of the Reynolds shear stress.

INTRODUCTION

A turbulent boundary layer (TBL) subjected to a strong or prolonged adverse pressure gradient (APG) develops a large mean velocity defect. The mean shear rates in the outer region are no longer small in comparison to their near-wall counterparts while near the wall, the importance of viscous forces and of the wall shear stress diminishes. As a result, in contrast to canonical wall-bounded turbulent flows, the near-wall turbulent kinetic energy production peak is absent or very small and the main production peak is found in the outer region of the flow (Skåre & Krogstad, 1994; Na & Moin, 1998; Elsberry *et al.*, 2000). By analysing several large-velocity-defect TBLs, Gungor *et al.* (2014) have concluded that these boundary layers are globally less efficient in extracting turbulent energy from the mean flow than the zero-pressure gradient (ZPG) TBL. The Reynolds stresses and the production of turbulent kinetic energy were found to be weaker in the lower half of the large-velocity-defect boundary layers than in the ZPG TBL. Furthermore, the outer-region turbulent statistics of TBLs close to detachment were found to resemble those of single-stream mixing layers. These various observations suggest that the physical mechanisms and coherent structures responsible for the production and transport of turbulence might be different.

Unfortunately, detailed analyses of the coherent structures found in APG TBLs are rare. By analyzing the DNS data of a turbulent separation bubble of Na & Moin (1998), Chong *et al.* (1998) suggested that in the APG zone prior to detachment more of the eddies which contribute to the Reynolds shear stress are eddies which are not connected to the wall. In the case of an equilibrium APG TBL, Krogstad & Skåre (1995) found that the lower part of the boundary layer is strongly dominated by Q4 motions, while in a ZPG TBL second and fourth quadrant events are equally important. The streamwise correlation length of u was also found to be considerably shorter in the APG case throughout the boundary layer, a result also obtained later in different large-velocity-defect TBLs by Rahgozar & Maciel (2012) and Gungor *et al.* (2014). Rahgozar & Maciel (2011) observed that the predominance of streaky u-structures in the outer region of a large-velocity-defect TBL is less than in the ZPG case. This predominance even disappears near detachment. By analysing the same flow, Rahgozar & Maciel (2012) found that large-scale u-structures are less elongated than those of ZPG TBLs, especially in the lower part of the boundary layer.

Quadrant analysis in the plane of streamwise and wall-normal velocity fluctuations (u,v) has been used extensively in the past to investigate the bursting process close to the wall (Robinson, 1991). Later this type of analysis was extended to study the outer structures (Wark & Nagib, 1991; Lozano-Durán *et al.*, 2012). Coherent and intense Q2 and Q4 events carry most of the Reynolds shear stress and as such they play a crucial role in terms of momentum flux and production of turbulent energy (Lozano-Durán *et al.*, 2012). Therefore, it is clear that their study is fundamental to increase the comprehension and subsequent control of these turbulent flows. It is thus only natural to extend the quadrant analysis to three-dimensional structures as was first done for channels by Lozano-Durán *et al.* (2012) (hereafter referred to as LFJ) and as is done in this article for an APG flow. Understanding the three-dimensional organization and dimensions of the structures related to the Reynolds

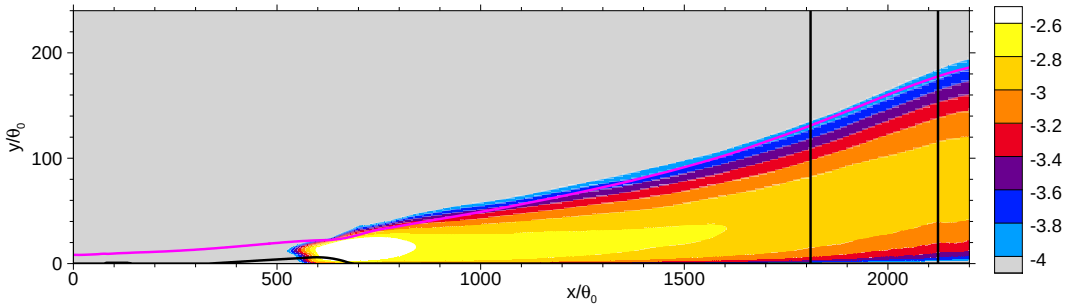

Figure 1. Contours of $\log_{10}(-\langle uv\rangle/U_{e_0}^2)$ in the lower half of the domain. The axes are not to scale. The black contour line is the zero contour of the streamwise mean velocity U, and marks locations of the trip element ($80 \le x/\theta_0 \le 130$) and the separation bubble. The solid magenta line shows the boundary layer thickness. The vertical black lines are the selected two stations where $(Re_\theta, H) = (1755, 2.0)$ and $(2175, 2.5)$ respectively.

shear stress is a further step but certainly not the last one in learning how turbulent wall bounded flows are organized.

LFJ called Qs the quadrant-splitted three-dimensional *uv* structures. They found that wall-detached Qs are background stress fluctuations while wall-attached Qs are bigger and carry most of the Reynolds shear stress in channel flows. The number of wall-attached Qs decreases away from the wall, but the fraction of Reynolds shear stress that they carry is independent of their size and location. More recently, Lozano-Durán & Jiménez (2014) studied the time evolution of these Qs. They found that wall-attached Q2s and Q4s are essentially mirror images of each other and they suggested that they are both manifestations of a single quasi-streamwise roller lying between them. They also showed that their dynamics is controlled by the local mean shear and that most of them are not born close to the wall.

In the present work, the geometric and kinematic characteristics of Q structures in a strongly decelerated non-equilibrium boundary layer is investigated to advance our knowledge and understanding of APG boundary layer flows. Some comparisons with the results obtained by LFJ are made.

METHODOLOGY

Numerical Methodology

The database used in the present study was obtained via direct numerical simulation (DNS) by Gungor *et al.* (2014). The DNS was performed with a parallelpiped domain over a smooth no-slip wall, with spanwise periodicity and streamwise non-periodic inflow and outflow. The Navier-Stokes equations were integrated using a fractional step method on a staggered grid, with third-order Runge-Kutta time-integration, fourth-order compact spatial discretization for the convective and viscous terms, and second-order discretization for the pressure in the directions perpendicular to the span, which is spectral. The computational box dimensions are $(L_x, L_y, L_z)/\theta_0 = (2380, 450, 1100)$, where θ_0 is the momentum thickness measured at the inflow, corresponding to $1537 \times 201 \times 768$ grid points. The resolutions in wall units at $Re_\theta = 2175$ are $(\Delta x_g^+, \Delta y_{g,min}^+, \Delta z_g^+) = (2.2, 0.2, 2.0)$. The coarsest resolution along x and z in terms of the Kolmogorov length η is found near the wall at reattachment, where $\Delta x_g/\eta \approx 10$.

The desired constant streamwise velocity gradient is controlled by imposing a constant uniform suction at the top simulation boundary. The streamwise and spanwise velocities at the top boundary satisfy free-slip conditions. The laminar Hiemenz profile is prescribed at the inflow and the velocities at the outflow are estimated by a convective boundary condition, with small corrections to enforce global mass conservation (Simens *et al.*, 2009). Transition is triggered by a disturbance strip located close to the inflow and modeled using the immersed boundary method (Simens & Gungor, 2013).

Flow Description

The flow is initially laminar, separates, transitions within the separation bubble, reattaches and develops into an attached turbulent APG boundary layer, the latter being the flow zone of interest for this study. The disturbance strip located upstream of the bubble does not cause the flow transition but it generates perturbations that hasten the bubble reattachment (Simens & Gungor, 2013). Figure 1 shows the distribution in the lower half of the domain of the logarithm of the Reynolds shear stress normalized with the square of the inflow freestream velocity. The logarithm is used in order to reveal better the wall-normal variation in the downstream region where the Reynolds shear stress has globally decreased. The time-averaged separated region and the boundary layer growth are also indicated in the same figure with thick solid lines. The shear layer formed by the separation bubble becomes unstable and sheds large, spanwise vortices. The large amplitude Reynolds shear stress seen in figure 1 around $x/\theta_0 = 700$ are due to the regular shedding of these vortical structures. The Reynolds shear stress decreases downstream and its wall-normal distribution becomes typical of large-velocity-defect TBLs near the end of the solution domain, with a wall-normal maximum in the middle of the boundary layer. By analyzing two-point cross-correlation coefficients, Gungor *et al.* (2014) found that the influence of the separated region continues up to $x/\theta_0 \approx 1800$ and only becomes small beyond that location. The attached turbulent boundary layer is still recovering from the effects of the shear layer instability all the way up to the end of the computational domain. The present study focuses on the region beyond $x/\theta_0 = 1550$ where these effects are relatively small but have nonetheless to be taken into account.

Figure 2 shows the streamwise evolution, in the region downstream of the separation bubble, of the external velocity U_e, the shape factor H and of two outer-region pressure gradient parameters: $\beta_{zs} = -(\delta/U_{zs})(dU_e/dx)$,

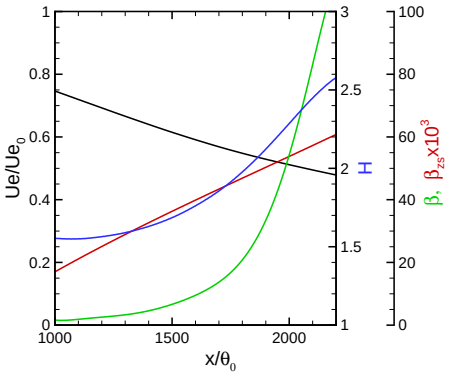

Figure 2. Streamwise evolution, downstream of the separation bubble, of: U_e/U_{e_0}, black; $\beta_{zs} \times 10^3$, red; β, green; H, blue.

where $U_{zs} = U_e\delta^*/\delta$ is the Zagarola-Smits velocity, and Rotta-Clauser's pressure gradient parameter $\beta = -(\Delta/u_\tau)(dU_e/dx)$, where $\Delta = \delta^* U_e/u_\tau$ is the Rotta-Clauser length scale. β is the traditional pressure gradient parameter that assumes the outer region velocity scale to be u_τ. Because of flow curvature introduced by the outlet and top boundary conditions, U_e does not decrease linearly. But interestingly, the flow conditions lead to a pressure gradient parameter β_{zs} that increases in an almost linear fashion. Correspondingly, the rapid increase of H is indicative of the strong non-equilibrium nature of the flow.

Extraction of Q Structures

Since we would like to consider Q structures in an APG boundary layer in the absence of large-scale perturbations and at a sufficiently high Reynolds number, the region of the flow used for the extraction of the Qs starts at $x/\theta_0 = 1546$ and ends at $x/\theta_0 = 2180$ ($Re_\theta = 1314 - 2207$). In this region, the boundary layer is in strong non-equilibrium state and possesses a large mean velocity defect ($H = 1.72 - 2.56$). The box covers $\delta_{0.995}/\theta_0 \approx 97 - 184$, with an average of $\delta_a/\theta_0 = 140.7$. The box dimensions for the extraction of the Q structures are $(B_x, B_y, B_z)/\delta_a = (4.5, 2, 8.0)$.

The procedure adopted to identify the Qs follows the method used by LFJ. The Qs are defined as regions of connected points that satisfy simultaneously two conditions. The first condition is $|u(\mathbf{x})v(\mathbf{x})| > H^* u'v'$, where u' and v' are respectively the streamwise and wall-normal standard deviations of velocity fluctuations and H^* is the threshold constant, also called hyperbolic-hole size. The second condition is that all points within a Q structure are in the same quadrant of the u, v space. Point connectivity is defined with the six orthogonal neighbours. Following the notation of LFJ, the Q2 and Q4 structures will be referred as Q^-, and the Q1s and Q3s as Q^+ hereafter.

As in LFJ a percolation analysis has been performed to determine a value for H^* that gives an equilibrium between detecting only a few very big objects and detecting only a few small and very intense Qs. In contrast to LFJ, the percolation test was performed for each Q type separately. The results shown in figure 3 are averages over 31 fields of the parameters. Since the Qs are identified according to their uv quadrant, the ratio of the volume of the largest Q in one field, V_{lar}, to the volume of all identified Qs in that field, V_{tot}, does not tend to one as H^* decreases. Qs

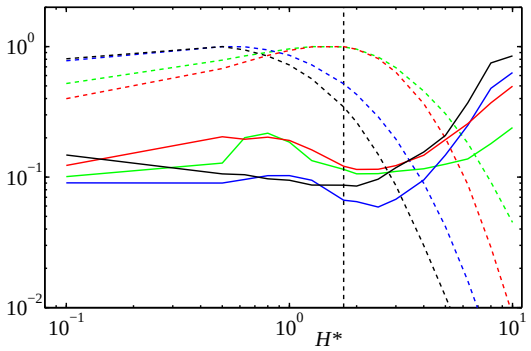

Figure 3. Percolation diagram for the identification of Qs: Q1, blue; Q2, red; Q3, black; Q4, green. Average over 31 fields of: V_{lar}/V_{tot}, solid lines; N/N_{max}, dashed lines. The vertical dashed line indicates the chosen hyperbolic hole size of $H^* = 1.75$.

of quadrant i cannot fill the space since $(uv)_i = 0$ at points where the quadrant is not i. Moreover, Qs of a given type remain disconnected when H^* is decreased since they are surrounded by Qs of other types. Consequently, the ratio V_{lar}/V_{tot} seems to saturate as H^* is decreased, meaning that the size of the Qs no longer varies significantly. Nevertheless, a percolation crisis seems to take place in the approximate range $1.2 \leq H^* \leq 2.5$ for Q1, Q2 and Q4. A hyperbolic hole size of $H^* = 1.75$ is chosen because it is in the middle of this range and it maximizes the number of Q^-s. It is the same value as used by LFJ in turbulent channel flows.

The linear dimensions of the Qs are defined with a rectangular box circumscribing them, the sides of this box being denoted as Δx, Δy and Δz and the midheight position of the box y_c. Structures that are as long as the streamwise length of the extraction box, $\Delta x = B_x$, are disregarded because the length of these structures is undetermined. Similarly, very small Qs with a volume $V < (\Delta x_g)^3$ are rejected because their sizes are not well resolved on the numerical grid. Furthermore, only Qs whose center is below the boundary layer thickness, $y_c/\delta_a \leq 1$, are considered to facilitate a comparison with channel flow.

RESULTS

Before analysing the Q structures, some turbulence statistics are presented in figure 4 in order to appreciate the difference between the present large-defect boundary layer and canonical wall flows. The figure shows the profiles of the Reynolds shear stress at two streamwise locations corresponding to $H = 2, Re_\theta = 1755$ and $H = 2.5, Re_\theta = 2175$. They are compared to a profile of the ZPG TBL of Simens *et al.* (2009) at a comparable Reynolds number ($Re_\theta = 1975$). The Reynolds shear stress is normalised with the outer velocity scale U_{zs}. In the present large-defect TBL, the maximum of the Reynolds shear stress is not near the wall like in canonical wall flows, but rather in the middle of the boundary layer. The Reynolds shear stress decreases in the lower half of the boundary layer as the velocity defect increases. All these characteristics are commonly found in large-defect TBLs (Gungor *et al.*, 2014).

The difference between ZPG and large-defect APG TBLs is even more pronounced for the production of turbulent kinetic energy, also shown in Fig. 4. In large-defect

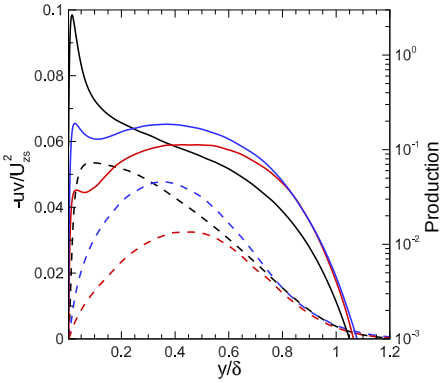

Figure 4. Reynolds shear stress, dashed lines, and production of turbulent kinetic energy, solid lines, normalized with U_{zs} and δ. Present flow: $H = 2$, blue; $H = 2.5$, red. ZPG TBL (Simens *et al.*, 2009), black.

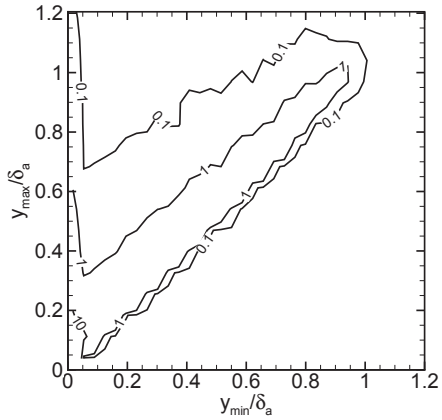

Figure 5. Joint pdf of y_{min}/δ_a and y_{max}/δ_a for Q$^-$s. Contour levels are 0.1, 1 and 10.

APG TBLs, the maximum production is in the outer region and production in the upper half of the boundary layer is comparable to that of ZPG TBLs when scaled properly (Gungor *et al.*, 2014). A near-wall production peak exists in the present flow even at the position corresponding to $H = 2.5$ but it is two orders of magnitude smaller than in the ZPG TBL at that position and four times smaller than the outer peak. Since U_{zs} is proportional to the mean shear rates present in the outer region, figure 4 indicates that the present large-defect TBL is globally less efficient in extracting turbulent energy from the mean flow than the ZPG one. Note that Gungor *et al.* (2014) have shown that for two other types of large-defect TBLs, the Reynolds stresses and production of k do not exceed those of the ZPG TBL in the outer region (when normalized with U_{zs} and δ). The higher outer levels found in the present flow could be due to the presence of the shear layer instability upstream.

The intense Reynolds shear stress coherent structures are now analysed keeping the previous observations in mind. With the extraction procedure defined in the previous section, a total of 1.3×10^6 Qs are identified in 460 statistically independent velocity fields. Of those, 56% are Q$^-$ structures. Figure 5 shows the joint probability density function (pdf) of the minimum and maximum wall distances for the Q$^-$s. The structures separate into two groups: wall-attached and wall-detached structures. The wall-attached Q$^-$s form the narrow vertical band with $y_{min} < 0.05\delta_a$ of the joint pdf, while wall-detached structures form the wide diagonal band. Figure 5 shows that the height of wall-attached Q$^-$s can exceed the boundary layer thickness. Wall-attached Q$^-$s as tall as approximately $2\delta_a$ are found. When comparing with similar joint pdfs of the Q$^-$s of LFJ for channel flows, it is found that in the present APG flow the probabilities are higher everywhere, except near the origin. This implies that, in proportion, there are definitely less small Q$^-$s close to the wall in the APG TBL than in channel flows. Such a result is expected since turbulence activity is significantly reduced near the wall in comparison.

Table 1 summarizes the number and volume fractions for the various types of Qs. Like in channel flow, Q$^+$s are less frequent than Q$^-$s, and they occupy a very small fraction of the space, 0.7% against 4% for Q$^-$s. Although the number fraction of Q2s and Q4s is comparable between the channel flow and the present flow, the volume occupied by these structures is much less for the large-defect TBL. In particular, Q2s in the TBL occupy less than half the space of Q2s in channel flow. But one as to keep in mind that in the case of the TBL, about half the volume of the extraction box is the freestream, non-turbulent flow.

Wall-attached Q2s and Q4s represent 36% of the total number of Q$^-$s and 64% of their volume. In channel flow, these percentages are respectively about 44% and 77%. The number and size proportions of attached Q$^-$s are therefore reduced in a large-velocity-defect boundary layer. Q structures whose center is in the range $0.2 < y_c/\delta_a < 0.6$ were also analysed separately. They are important because $0.2 < y/\delta < 0.6$ corresponds to the region of maximum turbulence intensity, Reynolds shear stress and turbulent kinetic energy production (see Fig. 4). In that range, 94% of the Q$^-$s are detached structures.

Figure 6 shows the fraction of the Reynolds shear stress carried by the various types of attached and detached Qs at the position corresponding to $H = 2.5$. With the threshold value chosen for the extraction of the Qs ($H^* = 1.75$), the identified Q$^-$ structures carry 25 to 45% of the Reynolds shear stress. Attached Q$^-$s dominate in the lower half of the boundary layer, especially near the wall, and attached Q4s contribute more than attached Q2s. The latter result can be put in line with what Krogstad & Skåre (1995) have found for single-point quadrant events: Q4 motions clearly dominate in the lower part of an equilibrium APG TBL contrary to the ZPG TBL where Q2 and Q4 motions are equally important. In the upper half region, detached Q2s gain importance and contribute more than attached Q2s. All types of Q$^-$s contribute significantly in the middle of the boundary layer.

Figure 7 presents a comparison between the fraction of the Reynolds shear stress carried by the various Qs in the present flow and in channel flow. To simplify the reading of the plots, Q1s and Q3s are grouped together, and so are detached Q2s and Q4s. Q$^-$s in the channel flow carry more of the Reynolds shear stress than those in the present flow. Less intense *uv* motions therefore play a more important role in large-defect TBLs. The main reason for this difference resides in the much smaller contribution of attached Q2s in the present flow which is not compensated by the increase in the contribution of detached Q$^-$s. Detached Q2s and Q4s indeed play a more important role in the present flow and they even become dominant above 0.5δ.

Table 1. Number fraction with respect to total number of Qs, and volume fraction with respect to extraction zone volume ($B_x \times B_y \times B_z$) for the four different types of Qs. Channel at $Re_\tau = 950$ (LFJ).

Case	N_1	N_2	N_3	N_4	V_1	V_2	V_3	V_4
Present (all)	0.24	0.28	0.20	0.28	0.003	0.024	0.004	0.015
Present (attached)	0.06	0.09	0.03	0.10	0.001	0.015	0.000	0.010
Channel (all)	0.18	0.33	0.19	0.31	0.004	0.056	0.006	0.025
Channel (attached)	0.02	0.15	0.006	0.13	0.000	0.047	0.000	0.015

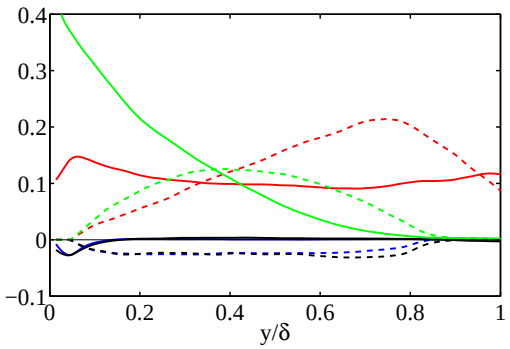

Figure 6. Fraction of the Reynolds shear stress at $Re_\theta = 2175$ ($H = 2.5$) from attached Qs, solid, and detached Qs, dashed. Q1, blue; Q2, red; Q3, black; Q4, green.

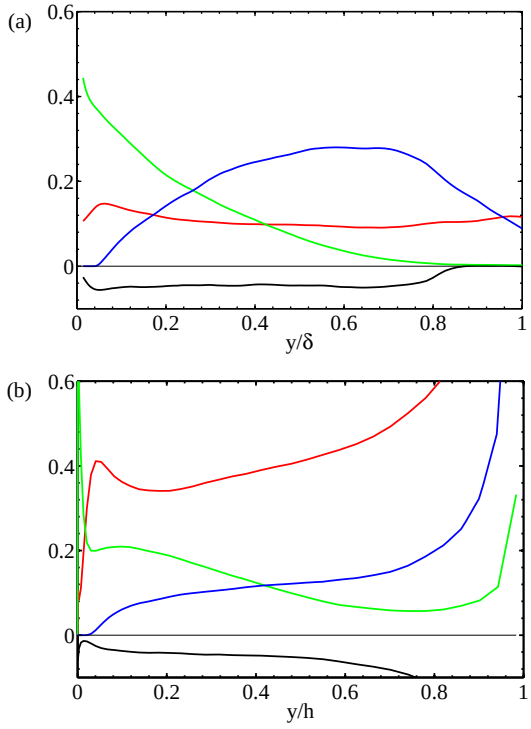

Figure 7. Fraction of the Reynolds shear stress from: attached Q2s, red; attached Q4s, green; detached Q$^-$s, blue; all Q$^+$s, black. (a) present flow at $Re_\theta = 2175$ ($H = 2.5$) , (b) channel flow at $Re_\tau = 950$ of LFJ.

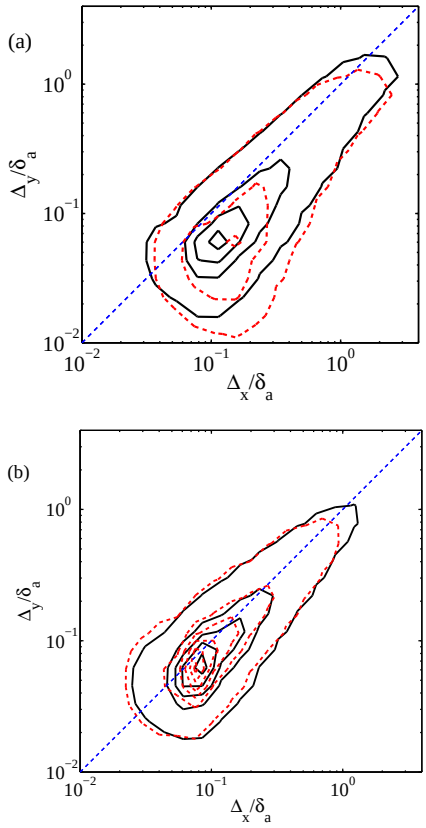

Figure 8. Joint pdfs $p(\Delta_x/\delta_a, \Delta_y/\delta_a)$ of the logarithms of the sizes of the boxes circumscribing Q$^-$s: (a) wall-attached Q$^-$s, (b) wall-detached Q$^-$s. The straight dashed lines are $\Delta_y = \Delta_x$.

The amount of Reynolds shear stress they carry is higher than that of similar structures in channel flow.

Figure 8 presents joint pdfs of the logarithms of the streamwise and wall-normal sizes, normalized with δ_a, of the boxes circumscribing Q2s and Q4s for attached (a) and detached structures (b). Like in LFJ for turbulent channel flows, the Q2 and the Q4 structures have similar sizes, with Q2s slightly bigger. The detached structures are approximately as long as they are tall and wide, $\Delta_x \approx \Delta_y \approx \Delta_z$, while attached Q$^-$s tend to be more elongated in the streamwise direction, by a factor of almost 2 ($\Delta_x \approx 2\Delta_y \approx 2\Delta_z$). This elongation is however not as pronounced as in channel flows, where LFJ found attached Q$^-$s to be 3 times longer than tall and wide for all sizes. In Krogstad & Skåre (1995), Lee & Sung (2009) and Rahgozar & Maciel (2012), it was also observed that above a certain height the length of the

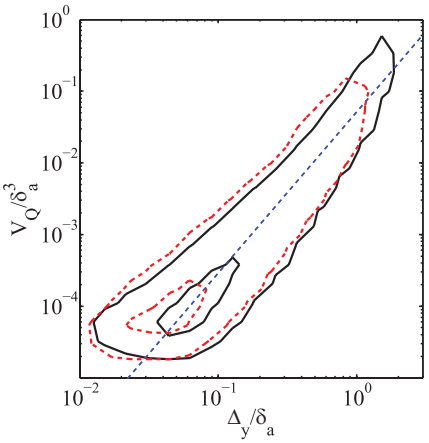

Figure 9. Joint pdfs of the logarithms of the volume V_Q/δ_a^3 and of the height Δ_y/δ_a for wall-attached Q$^-$s. The dashed straight line corresponds to $V_Q \propto \Delta_y^{2.25}$.

u-structures becomes shorter in an APG flow in comparison with a ZPG flow.

The largest structures are attached Q2s that can reach $\Delta_x \approx 3\delta_a$ and $\Delta_y \approx \Delta_z \approx 2\delta_a$. For channel flows, LFJ found very long attached Q2s reaching $\Delta_x \approx 20h$ and $\Delta_y \approx \Delta_z \approx 2h$. The rapid streamwise variations and strong non-equilibrium state of the present APG TBL probably prohibit the existence of such long motions. The detached Q$^-$s are globally smaller than their attached counterparts, but not significantly. Detached Q$^-$s whose center is in the range $0.2 < y_c/\delta_a < 0.6$ have a distribution of dimensions (not shown) similar to that of the ensemble of all detached Q$^-$s.

Figure 9 shows the joint pdfs of the volumes and heights of the attached Q2s and Q4s. The attached Q2s and Q4s follow reasonably well the relation $V_Q \propto \Delta_y^{2.25}$ proposed by LFJ. They interpreted it as an estimate of the fractal dimension of the structures but they also characterized the shapes of the Qs by more direct methods. They showed that the attached Q2s and Q4s found in channel flows resemble sponges formed by the agglutination of flakes. Inspection of individual attached Q$^-$s confirms that their shape is similar in the present flow. Moreover, the large detached Q$^-$s have shapes similar to the attached ones.

CONCLUSIONS

Wall-attached and wall-detached Q$^-$ structures are detected everywhere in the present large-defect boundary layer. Wall-attached Q$^-$s occupy less space and are much less streamwise elongated than those found in turbulent channel flows by LFJ. In channels, LFJ observed that the detached Qs represent background fluctuations of small size, of the order of a few Kolmogorov lengths, whose contributions to the Reynolds shear stress almost cancel. In the present flow, detached Q$^-$ structures are comparable in size to attached Q$^-$s and they carry a significant amount of the Reynolds shear stress throughout the outer region. In the zone of maximum turbulence intensity, Reynolds shear stress and turbulent kinetic energy production of the present flow, approximately $0.2 < y/\delta < 0.6$, 94% of the Q$^-$s are detached ones. Moreover, in that region, the detached Q$^-$s contribute as much to the Reynolds shear stress as the attached ones.

ACKNOWLEDGMENTS

Funded in part by the Multiflow program of the European Research Council. AGG and YM were supported in part respectively by ITU-BAP and NSERC of Canada. The authors would like to thank Prof. Jiménez for organizing the First Multiflow Summer Workshop and Adrián Lozano-Durán and Prof. Jiménez for providing their data and the processing programs for the Q structures analysis.

REFERENCES

Chong, M. S., Soria, J., Perry, A. E., Chacin, J., Cantwell, B. J. & Na, Y. 1998 Turbulence structures of wall-bounded shear flows found using DNS data. *Journal of Fluid Mechanics* **357**, 225–247.

Elsberry, K. Loeffler, F., Zhou, M.D. & Wygnanski, I. 2000 An experimental study of a boundary layer that is maintained on the verge of separation. *J. Fluid Mech.* **423**, 227–261.

Gungor, Ayse G., Maciel, Yvan, Simens, Mark P. & Soria, Julio 2014 Analysis of a turbulent boundary layer subjected to a strong adverse pressure gradient. *Journal of Physics: Conference Series* **506**, 012007.

Krogstad, P. Å. & Skåre, P. E. 1995 Influence of a strong adverse pressure gradient on the turbulent structure in a boundary layer. *Phys. Fluids* **7**, 2014–2024.

Lee, J. H. & Sung, H. J. 2009 Structures in turbulent boundary layers subjected to adverse pressure gradients. *J. Fluid Mech.* **639**, 101–131.

Lozano-Durán, A., Flores, O. & Jiménez, J. 2012 The three-dimensional structure of momentum transfer in turbulent channels. *J. Fluid Mech.* **694**, 100–130.

Lozano-Durán, A. & Jiménez, J. 2014 Time-resolved evolution of coherent structures in turbulent channels: characterization of eddies and cascades. *Journal of Fluid Mechanics* **759**, 432–471.

Na, Y. & Moin, P. 1998 Direct numerical simulation of separated turbulent boundary layer. *J. Fluid Mech.* **374**, 379–405.

Rahgozar, S. & Maciel, Y. 2011 Low-and high-speed structures in the outer region of an adverse-pressure-gradient turbulent boundary layer. *Experimental Thermal and Fluid Science* **35** (8), 15751587.

Rahgozar, S. & Maciel, Y. 2012 Statistical analysis of low-and high-speed large-scale structures in the outer region of an adverse pressure gradient turbulent boundary layer. *Journal of Turbulence* **13**, 1–24.

Robinson, S. K. 1991 Coherent Motions in the Turbulent Boundary Layer. *Annu. Rev. Fluid Mech.* **23** (1), 601–639.

Simens, M.P. & Gungor, A.G. 2013 The effect of surface roughness on laminar separated boundary layers. *Journal of Turbomachinery,doi:10.1115/1.4025200* .

Simens, M.P., Jiménez, J., Hoyas, S. & Mizuno, Y. 2009 A high-resolution code for turbulent boundary layers. *Journal of Computational Physics* **228**, 4218–4231.

Skåre, P. E. & Krogstad, P. Å. 1994 A turbulent equilibrium boundary layer near separation. *J. Fluid Mech.* **272**, 319–348.

Wark, C. E. & Nagib, H. M. 1991 Experimental investigation of coherent structures in turbulent boundary layers. *J. Fluid Mech.* **230**, 183–208.